

Geometrical-confinement effects on excitons in quantum disks

Jakyoung Song and Sergio E. Ulloa

Department of Physics and Astronomy and Condensed Matter and Surface Sciences Program

Ohio University, Athens, Ohio 45701-2979

Abstract

Excitons confined to flat semiconductor quantum dots with elliptical cross section are considered as we study geometrical effects on exciton binding energy, electron-hole separation, and the resulting linear optical properties. We use numerical matrix diagonalization techniques with appropriately large and optimized basis sets in an effective-mass Hamiltonian approach. The linear optical susceptibilities of GaAs and InAs dots for several different size ratios are discussed and compared to experimental photoluminescence spectra obtained on GaAs/ $\text{Al}_x\text{Ga}_{1-x}\text{As}$ and InAs/GaAs quantum dots. For quantum dots with several nm in size, there is a strong blue shift of the luminescence due to geometrical confinement effects. Also, transition peaks are split and shifted towards higher energy, in comparison with dots with circular cross sections.

I. INTRODUCTION

The development of clever fabrication techniques in semiconductors has brought the reduction of the effective dimension of electronic states from their usual three-dimensional character in bulk materials, to “zero-dimensional” states in quantum dots.¹ The quantum effects of these lower-dimensional systems have attracted much attention in recent years, due in part to possible applications which include electronic devices based on parallel and perpendicular transport, quantum well lasers, and optical devices.² Two-dimensional quantum-well or quantum-film structures, which provide confinement in one space dimension, have been well investigated, and quantum exciton effects observable even at room temperature have been studied.³ The confinement of excitons has also been shown to result in very large electro-optical shifts of the absorption peaks, producing the so-called quantum-confined Stark effect.^{3,4}

In quasi-zero-dimensional quantum dot systems, the additional quantum confinement dramatically changes the optical and electronic properties, compared to those in higher-dimensional structures, as the whole single-particle spectrum is now discrete. Correspondingly, the excitonic spectrum is expected to be strongly affected. The properties of excitons confined in quantum boxes were first analyzed theoretically by Bryant,⁵ who used variational and configuration-interaction representations. Later on, excitons and biexcitons have been studied,^{6,7} as well as excitons in the presence of a strong magnetic field,⁸ using numerical matrix diagonalization schemes.

On the experimental side, interband optical spectroscopies, such as photoluminescence, have been used to study various quantum dot systems — such as those produced in the GaAs/Al_xGa_{1-x}As structure, with its bandgap modulation.⁹⁻¹¹ More recently, fascinating studies on so-called “self-assembled” quantum dots, such as InAs and In_xGa_{1-x}As clusters on GaAs substrates, have also been reported.¹²⁻¹⁵ Most of the theoretical investigations are based on the assumption that the shape of quantum dots is a simple sphere or box, having a great deal of symmetry, both because it simplifies calculations and because quantities such

as the exciton binding energy scale very well with the overall dot size. However, realistic dot shapes are probably much less symmetrical, as well as being typically flat and more two-dimensional in shape.^{12–15}

Here, we consider the effect that less symmetric structures, namely flat quantum dots with elliptical cross sections, or “elliptical quantum disks”, have on the excitonic optical properties. To date, little work has been reported on the properties of nonsymmetric quantum dots, probably because this system has more complicated solutions.^{13,15} Our studies within the effective mass approximation yield some very interesting consequences of the elliptical asymmetry: apart from the expected blue shift of the first excitonic transition for dots with the same overall area but different axes, we find a rearrangement of the oscillator strength which characterizes individual dot shapes. In particular, since elliptical cross-section dots have less symmetry, some of the accidental degeneracies in circular dots giving rise to stronger and fewer peaks in the imaginary part of the optical susceptibility are split. This gives rise to a more monotonically decreasing peak intensity for higher energy features in the susceptibility of noncircular dots. This behavior can in turn be used to structurally characterize specific dots from their photoluminescence excitation response.

The remainder of the paper is organized as follows. We introduce the theoretical method in Sec. II. Here, we outline the effective mass Hamiltonian approach and introduce the various basis function representations which allow us to use numerical methods to calculate the eigenvalues and eigenfunctions of excitons in these quantum dots. A great deal of care is needed to assure that the solutions obtained are well behaved and converged with a finite computational effort. We discuss in this section how this is accomplished. In Sec. III, we discuss the main geometrical effects on various exciton characteristics, such as the exciton binding energy, electron-hole separation, and the linear optical susceptibility. Solutions for excitons in quantum dots with both circular and elliptical cross sections are shown, using large enough basis sets, and a set of optimized basis functions, which improve the accuracy of the solutions at a modest computational cost. Finally, we summarize our conclusions in Sec. IV. The Appendix contains an outline of the derivation of the Coulomb matrix element

with these basis functions. The analytical expression presented there greatly simplifies our calculations.

II. THEORETICAL METHOD

For concreteness, and to simulate recent quantum dot systems,^{12–14} we assume quantum dots with an oblate spheroidal profile where the lateral xy confinement is much weaker (or larger size) than that along the z direction. Correspondingly, the electrons and holes are assumed confined in an effectively two-dimensional potential with a constant z profile, V_z . We assume V_z to be a hard-wall confinement potential, so that the z component of the energy is $\hbar^2\pi^2/2mL_z^2$, with $L_x, L_y \gg L_z$. Further, we approximate the single z wavefunction in the problem as a δ function centered at the origin, so that the problem can be described by a separable Hamiltonian in two dimensions. The lateral confinement is modeled via harmonic potentials with two different frequencies ω_x and ω_y , which yield the elliptical cross section of the dots with axes ratio given by $L_x/L_y = \sqrt{\omega_y/\omega_x}$, for both electrons and holes. The smoothly varying potential should mimic well the situation in experiments where the dots are effectively embedded in a dielectric matrix.^{1,12}

The effective-mass parabolic-band Hamiltonian for an electron-hole pair is given by $H = H_e + H_h + H_{e-h}$, where the subscripts e and h represent electron and hole, and

$$H_e = \frac{p^2}{2m_e} + \frac{1}{2}m_e\omega_x^2x_e^2 + \frac{1}{2}m_e\omega_y^2y_e^2 + V_{ze}, \quad (1)$$

with a similar expression for the Hamiltonian of the hole, H_h .¹⁶ The Coulomb interaction between electron and hole is screened by a background dielectric constant ϵ , so that $H_{e-h} = -e^2/\epsilon r_{e-h}$.

We rewrite the Hamiltonian into relative and center of mass coordinates, described by $\mathbf{r} = \mathbf{r}_e - \mathbf{r}_h$, and $\mathbf{R} = (m_e\mathbf{r}_e + m_h\mathbf{r}_h)/M$. The total and reduced masses are given by $M = m_e + m_h$, and $\mu = m_em_h/M$, respectively. The total Hamiltonian of this system can then be written in the form $H = H_{c.m.} + H_{rel}$, with the expected expressions

$$H_{c.m.} = \frac{P^2}{2M} + \frac{1}{2}M\omega_x^2 X^2 + \frac{1}{2}M\omega_y^2 Y^2 + V_Z, \quad (2)$$

and

$$H_{rel} = \frac{p^2}{2\mu} + \frac{1}{2}\mu\omega_x^2 x^2 + \frac{1}{2}\mu\omega_y^2 y^2 - \frac{e^2}{\epsilon\sqrt{x^2 + y^2}} + V_z. \quad (3)$$

The Hamiltonian of the center of mass is obviously a two-dimensional harmonic oscillator in the XY plane, with wavefunction $\Psi_{N_X N_Y} = \phi_{N_X}(X) \phi_{N_Y}(Y)$, and energy $E_{c.m.}$, where

$$\phi_N(X) = \left(\frac{\alpha_M}{\pi^{1/2} 2^N N!} \right)^{1/2} e^{-\alpha_M^2 X^2/2} H_N(\alpha_M X), \quad (4)$$

$\alpha_M = \sqrt{M\omega_x/\hbar}$, and

$$E_{c.m.} = \left(N_X + \frac{1}{2} \right) \hbar\omega_x + \left(N_Y + \frac{1}{2} \right) \hbar\omega_y + \frac{\hbar^2 \pi^2}{2ML_z^2}. \quad (5)$$

Here, N_X and N_Y are quantum numbers for the center of mass coordinate, and H_N is a Hermite polynomial.¹⁷

The physics of the problem is determined to a great extent by the ratio between the effective Bohr radius, $a_B^* = \hbar^2 \epsilon / \mu e^2$, and the size of the dot, $L = \sqrt{L_x L_y}$, where $L_i = \sqrt{\hbar / \mu \omega_i}$. The strong confinement limit for $L \leq a_B^*$ is characterized by a weak electron-hole correlation and by the Coulomb term being a small perturbation of the single-particle confined-level energy. On the other hand, the weak-confinement limit for $L \geq a_B^*$ reduces asymptotically to the problem of a free two-dimensional exciton for large L , where the Coulomb interaction dominates the state of the exciton¹.

With this in mind, the effects of the Coulomb term H_1 in $H_{rel} = H_0 + H_1$, are treated by using the solutions of H_0 as the basis set in the diagonalization of H_{rel} . The unperturbed Hamiltonian of the relative coordinate H_0 is also a two-dimensional harmonic oscillator, so that the wavefunction of the interacting electron-hole pair is described by a linear combination of wavefunctions, $\psi_{n_x n_y} = \phi_{n_x}(x) \phi_{n_y}(y)$, with the ϕ 's satisfying a similar expression to Eq. (4), and correspondingly

$$E_{rel}^0 = \left(n_x + \frac{1}{2} \right) \hbar\omega_x + \left(n_y + \frac{1}{2} \right) \hbar\omega_y + \frac{\hbar^2 \pi^2}{2\mu(2L_z)^2}, \quad (6)$$

where n_x and n_y are quantum numbers for the relative coordinate. (Notice z confinement length for this coordinate is $2L_z$.)

With this basis set, the interaction matrix elements of the electron-hole pair can be calculated analytically and expressed in terms of hypergeometric functions as outlined in the Appendix. This analytical expression greatly simplifies the calculation, as most of the computational time is spent on the calculation of the matrix elements rather than on the diagonalization of the matrix. The resulting Hamiltonian matrix is real, symmetric, and sparse. The energies and eigenfunctions are calculated from the numerical diagonalization of the matrix, for a given size of the basis. The diagonalization is repeated with larger basis sets until the desired convergence is achieved (see below).

A. Circular limit

As an additional test of our numerical procedures we use the resulting radial equation of the relative Hamiltonian for the circular dot case, $\omega_x = \omega_y = \omega$, which is then given by

$$H_{rel} = \frac{p^2}{2\mu} + \frac{1}{2}\mu\omega^2 r^2 - \frac{e^2}{\epsilon r}. \quad (7)$$

The resulting one-dimensional equation can be directly integrated numerically, as reported by Que.⁷ Furthermore, the problem can also be solved using a harmonic basis set of radial states as those described above. For a large enough basis set, this approach yields the same results as those obtained by direct numerical integration.⁷ Notice also that the large dot limit ($\omega \approx 1/L \approx 0$) is easily solved as an expansion in terms of the Laguerre polynomial-based solutions of the free exciton problem.⁷ This allows one to obtain very accurate solutions for $1/L \approx 0$ with little computation. These results, moreover, allow us to test the convergence of the irreducible two-dimensional nonsymmetric problem ($\omega_x \neq \omega_y$), as we discuss below.

B. Optimized basis

Solutions for these elliptic cylinderlike quantum dots are also carried out using an optimized basis set, as the solution method discussed above requires a rather large number of states for full convergence, especially for large dots. Here, one notices that for large dots it is the Coulomb interaction that dominates the exciton states (since confinement becomes less important). Correspondingly, we choose a set of optimized frequencies, Ω_x and Ω_y , which are larger than the original frequencies, ω_x and ω_y . The values of the Ω 's are determined variationally, and allow one to consider H -matrix systems that are much smaller than those required when one uses the ω basis. The physical reason for this is that as the dot size increases, the exciton size converges to a_B^{2D} (the radius of the free two-dimensional exciton), and one needs a large number of ω states to describe the small-scale structure of the exciton.

Notice that the harmonic Ω basis allows also an easy calculation of the H -matrix elements in this case, so that for example,

$$\begin{aligned} \langle n_x' n_y' | H_0 | n_x n_y \rangle_\Omega = & \left[\hbar\Omega_x(n_x + \frac{1}{2}) + \hbar\Omega_y(n_y + \frac{1}{2}) \right. \\ & - \frac{\hbar}{2\Omega_x}(\Omega_x^2 - \omega_x^2)(n_x + \frac{1}{2}) - \frac{\hbar}{2\Omega_y}(\Omega_y^2 - \omega_y^2)(n_y + \frac{1}{2}) \left. \right] \delta_{n_x', n_x} \delta_{n_y', n_y} \\ & - \frac{\hbar}{4\Omega_x}(\Omega_x^2 - \omega_x^2) \left[\sqrt{n_x(n_x - 1)} \delta_{n_x', n_x - 2} + \sqrt{(n_x + 1)(n_x + 2)} \delta_{n_x', n_x + 2} \right] \delta_{n_y', n_y} \\ & - \frac{\hbar}{4\Omega_y}(\Omega_y^2 - \omega_y^2) \left[\sqrt{n_y(n_y - 1)} \delta_{n_y', n_y - 2} + \sqrt{(n_y + 1)(n_y + 2)} \delta_{n_y', n_y + 2} \right] \delta_{n_x', n_x} . \quad (8) \end{aligned}$$

Notice this reduces to the obvious diagonal matrix for $\Omega \rightarrow \omega$. This expression allows one to evaluate the Hamiltonian matrix rather conveniently, even for this other basis set.

C. Exciton characteristics

The wavefunctions of the relative coordinate problem can then be written as $|\psi\rangle = \sum_{n_x n_y} a_{n_x n_y} |n_x, n_y\rangle$, with either the ω or Ω basis states, which can be used to study various characteristic properties of the exciton system. For example, the mean electron-hole separation r_s , is given by

$$\begin{aligned}
r_s^2 = \langle \psi | r^2 | \psi \rangle &= \sum_{n_x n_y} \left[\frac{\hbar}{\mu \Omega_y} (n_y + \frac{1}{2}) + \frac{\hbar}{\mu \Omega_x} (n_x + \frac{1}{2}) \right] |a_{n_x, n_y}|^2 \\
&+ \frac{1}{2} \frac{\hbar}{\mu \Omega_y} \left[\sqrt{(n_y + 2)(n_y + 1)} a_{n_x, n_y+2}^* + \sqrt{n_y(n_y - 1)} a_{n_x, n_y-2}^* \right] a_{n_x, n_y} \\
&+ \frac{1}{2} \frac{\hbar}{\mu \Omega_x} \left[\sqrt{(n_x + 2)(n_x + 1)} a_{n_x+2, n_y}^* + \sqrt{n_x(n_x - 1)} a_{n_x-2, n_y}^* \right] a_{n_x, n_y}, \quad (9)
\end{aligned}$$

which gives an idea of the exciton size.

One can also use the diagonalization results to calculate directly measurable properties, such as the linear optical susceptibility of the quantum dot/disk. The linear optical susceptibility is proportional to the dipole matrix elements between one electron-hole pair j state and the vacuum state, $\langle 0 | P | 1 \rangle_j$.⁵ These in turn are proportional to the interband matrix element, p_{cv} ,¹⁸ which is the matrix element formed between an electron and hole in the conduction and valence bands, respectively. The form of the dipole matrix elements for a single exciton in the envelope function approximation is given by^{5,7}

$$|\langle 0 | P | 1 \rangle|^2 = |p_{cv}|^2 |\psi(0)|^2 \left| \int \int \Psi(X_e, Y_e) dX_e dY_e \right|^2. \quad (10)$$

Here, the wavefunction for the relative coordinate is given as above, so that

$$|\psi(0)|^2 = (\mu/\hbar\pi) \sqrt{w_x w_y} \left| \sum_{n_x n_y} (2^{n_x+n_y} n_x! n_y!)^{-1/2} a_{n_x n_y} \right|^2, \quad (11)$$

where the $a_{n_x n_y}$ coefficients are obtained from the diagonalization of the relative-coordinate Hamiltonian, and

$$\left| \int \int \Psi(X_e, Y_e) dX_e dY_e \right|^2 = 4\pi^2 \hbar N_X! N_Y! \left[\pi M \sqrt{w_x w_y} 2^{N_X+N_Y} (N_X/2)!^2 (N_Y/2)!^2 \right]^{-1}, \quad (12)$$

with $N_X = \text{even}$ and $N_Y = \text{even}$, for nonzero matrix elements. Finally, the dipole matrix elements have the form

$$|\langle 0 | P | 1 \rangle|^2 = 4 |p_{cv}|^2 \frac{\mu}{M} N_X! N_Y! \left[2^{N_X+N_Y} (N_X/2)!^2 (N_Y/2)!^2 \right]^{-1} \left| \sum_{n_x n_y} (2^{n_x+n_y} n_x! n_y!)^{-1/2} a_{n_x n_y} \right|^2. \quad (13)$$

The linear optical susceptibility can then be calculated from

$$\chi(\omega) = \sum_j |\langle 0|P|1\rangle_j|^2 (\hbar\omega - E_j - i\hbar\Gamma)^{-1}, \quad (14)$$

where Γ is introduced as a phenomenological level broadening constant.

Notice also that since experimental systems are typically configured to analyze a large collection of nearby dots, one should in principle be concerned by the effect of local fields. However, in typical experimental systems so far, where the separation between dots can be several microns, it is valid to assume that dots are basically independent. In the case of higher-dot densities, however, the dynamical response of the system may be affected by the local fields produced by neighboring dots, and one can obtain that response from the individual microscopic polarizabilities.¹⁹

III. RESULTS

As an interesting example of a typical system, we use parameters to describe GaAs quantum dots, so that the dielectric constant is $\epsilon = 13.1$, and the carrier masses are $m_e = 0.067m_0$, and (the heavy hole effective mass) $m_{hh} = 0.37m_0$.¹⁶ We present the numerical results for heavy-hole excitons in GaAs quantum dots with elliptical and circular cross sections. The solutions can be calculated using a sufficiently large basis set and/or an optimized basis set, as described above. Results obtained from these methods and different basis sets are shown in Fig. 1. The exciton binding energy and normalized electron-hole separation are shown as a function of quantum dot size ranging from 2 to 100 nm.

In the insets, results are shown for *circular* dots, with dot, dashed, and dot-dashed curves showing results for basis sets with $M = 30, 100$, and 500 wavefunctions, respectively. Here, states with n and n' from 0 to 29, 99, and 499 are used in Eq. (7). (The matrix size is obviously $M \times M$, and is diagonalized by a QL decomposition technique.²⁰) The results of the one-dimensional radial equation in the weak-confinement limit are shown with the solid line for comparison, and represent the exact quantity (both E_b and r_s) for large L . The transition between the strong and weak confinement regimes comes appropriately when the size of the quantum dot is near the effective Bohr radius, $L \approx a_B^* = 12.2$ nm. Notice that

it is for $L \approx 15$ nm that the $M = 100$ curve (dashed) departs from the exact result (solid line), and that one requires larger M values as L increases to achieve better convergence. The $M = 500$ basis set (dot-dashed curve) yields the convergent solutions with acceptable accuracy and execution time for a larger range of L values (≤ 60 nm). Similar behavior can be seen in the electron-hole separation in the ground state [inset in panel (b)].

The inset in 1(a) also shows the difference between the ω basis and Ω basis results. Diamonds show results for the $M = 400$ basis set with optimized Ω frequency, while triangles show results for $M = 400$ with the original ω basis set. For both cases, the states with n_x , n_y , n_x' , and n_y' from 0 to 19, respectively, are included for the $M = 400$ basis set (see Eq. 8). These states are used as the basis set for elliptical quantum dots. The results with the optimized basis set are essentially identical to the convergent solutions. The optimized frequencies used are also given as a function of dot size in the inset 1(a) (with $E_\Omega = \hbar\Omega$) as a long-dashed curve. For dot sizes 30 nm and larger, the optimized frequency Ω converges to 80 meV, corresponding to a dot size $L_\Omega = \sqrt{\hbar/\mu\Omega} = 4.1$ nm. This latter value is close to the two-dimensional effective Bohr radius ($a_B^{2D} = a_B^*/2\sqrt{2} = 4.3$ nm), as one would expect. Notice that for most of the range of L 's shown, one is in the weak-confinement regime, where $L \geq a_B^{2D}$. This is why the optimized basis set gives very reasonable results with minimal effort. It is also interesting that the agreement continues also for smaller dot sizes, completing the range from 2 to 100 nm. The exciton ground state binding energies and the normalized electron-hole separation obtained with the optimized Ω basis approach are basically exact to the fully converged results.

The main panels in Fig. 1 (a) and (b) show the geometrical confinement effects of excitons with several different size axis ratios in the xy plane. The plots show results versus $L = \sqrt{L_x L_y}$, the effective size of the dot, for $\omega_x/\omega_y = 1, 4$, and 9 ($L_y/L_x = 1, 2$, and 3) with diamonds, pluses, and triangles, respectively. The exciton binding energy increases for a small L as the axis ratio is increased; meanwhile, the normalized electron-hole separation is basically unchanged, except for small L values, where the confinement energy dominates. Notice that as the axis ratio increases, the single-particle and exciton states move up in

energy but the *binding* energy increases. This increase in binding energy for the elliptical dots is then related to the increase of the Coulomb energy *relative* to the confinement contribution to the total energy. (In fact, since r_s/L is basically unchanged with geometry, the Coulomb interaction energy is nearly constant in all these cases.)

To better explore the geometrical confinement effects on excitons, we show the linear optical susceptibility of the GaAs quantum disks with elliptical cross sections and lateral mean size of $L = \sqrt{L_x L_y} = 5$ nm (Fig. 2), and 10 nm (Fig. 3). The dot thickness along the z -direction is kept constant at $L_z = 3$ nm, and several size ratios for each axis in the xy plane are shown. We use here also a value for the optical bandgap of $E_g = 1.51$ eV. The results presented here were obtained using the optimized Ω basis set approach discussed above. Notice that since this function represents all of the possible transitions of this excitonic system, its features would be measurable via photoluminescence excitation measurements. On the other hand, the photoluminescence response would correspond to the first (lower energy) feature in these traces, associated with the ground state of the excitonic system.

Figure 2 shows the imaginary part of the linear optical susceptibility as a function of frequency for a dot with $L = \sqrt{L_x L_y} = 5$ nm (a broadening of $\Gamma = 2$ meV is used). The bottom trace is for a circular dot, so that $L_x = L_y = 5$ nm. The upper two traces show results for elliptical dots with a size ratio $L_y : L_x = 2 : 1$ ($L_y = 7.0$ nm, and $L_x = 3.5$ nm), and $3 : 1$ ($L_y = 8.7$ nm, $L_x = 2.9$ nm), respectively, all having the same mean size $L = 5$ nm. [Notice that although the peak heights are in arbitrary units, the ratio between different peaks or traces is real, reflecting the different dipole matrix elements involved.] One obvious difference among traces is that the first transition energy shifts to higher values by ≈ 26 and 69 meV, as the size ratio changes from 1:1 to 2:1 and 3:1, respectively. Notice that while increasing the size ratio, the exciton binding energies *increase* from 47 meV to 48 and 49 meV for each ratio. It is then clear that the larger blue shifts are due mostly to the increasing confinement as the disk becomes more elliptical, and not due to the binding energy between electron and hole. In all the cases shown, the transition involving the ground state of the exciton is dominant, as the excited states appear only with smaller oscillator

strength. Notice further that for the larger length ratio, the spectrum is understandably sparser, as the levels associated with the narrow dimension are quickly pushed upwards in energy. Finally, since the elliptical dots have lower symmetry, accidental degeneracies are fewer and the transition peaks show nearly monotonically decreasing intensities (unlike the circular dot case). [Notice these all the susceptibility traces include transitions between different center-of-mass states up to the $N_X = N_Y = 10$ levels. Additional N_X and N_Y values would yield higher energy structure.]

Figure 3 shows also the imaginary part of the susceptibility but for a dot size of 10 nm, and here with level broadening of 1 meV. The first transition energy in the circular quantum dot is 1.78 eV, while the values in the elliptical dots are 1.79 and 1.80 eV, for ratios 2 : 1 and 3 : 1. The transition energies result here to be lower than in Fig. 2 since the confinement is not as strong, reducing the effective gap energy. In this set of curves, the first transition energy (involving the ground state of the exciton) is shifted upwards for elliptical dots, due to the increased confinement, although the shift is not as large as in Fig. 2, since the overall lengths are larger. The first excited state appears split because the two-fold degeneracy of the excited state is broken as the dot becomes elliptical.

As dot size is increased, it is apparent that the geometrical effects are not as prominent, producing only a small shift of the spectrum of transitions. Incidentally, the onset of transitions for larger size dots ($L \approx 100$ nm) compares qualitatively well with experimental photoluminescence spectra in dots with similar disk geometry,¹⁰ where features appear in the energy range 1.73 – 1.74 eV, for dots with radius thought to be in the range 150–200 nm. According to the experimental results, the additional confinements give the observed blue shift, compared to two-dimensional quantum-well exciton case. Similarly, a blue shift appears due to the elliptical shape, although for $L \approx 100$ nm they are only ≤ 10 meV, as the size ratio increases to 2:1 and 3:1.

As an example of the effects for different materials, Fig. 4 shows the imaginary part of the susceptibility of InAs quantum dots with lateral mean size of 12 nm and thickness of 2.8 nm — having a dielectric constant $\epsilon = 14.6$, $m_e = 0.026m_0$, and heavy hole effective mass

$m_{hh} = 0.41m_0$. Here, the energy gap is taken as 0.43 eV, and we also use the optimized Ω basis set to obtain the results shown. The convergent optimized size, $L_\Omega = 10.5$ nm, is close to the two dimensional effective Bohr radius ($a_B^{2D} = 10.54$ nm). In this case, the first transition energy shifts to higher values by ≈ 11 and 28 meV, as the size ratio changes from 1:1 to 2:1 and 3:1, respectively. Notice the similarity with Fig. 2, although the energy scale and size (12 nm) are completely different here. This similarity is due to the scaling of the problem in terms of a_B^* . For these InAs parameters, $a_B^* = 29.8$ nm, so that $a_B^*/L \approx 2.5$, comparable to the value in Fig. 2 for GaAs, where $a_B^* = 12.2$, $L = 5$, and $a_B^*/L \approx 2.4$.

IV. CONCLUSIONS

We have demonstrated that strong geometrical confinement effects appear on excitons in GaAs and InAs quantum dots with elliptical cross sections. The solutions have been obtained using sufficiently large basis sets as well as with an optimized basis set. The results obtained with the optimized basis sets, such as exciton binding energy and normalized electron-hole separation, are extremely close to the best converged results, and only with a relatively modest computational effort.

The linear optical susceptibilities are calculated for several different lateral size ratios of each axis (x and y). Strong blue shifts in the susceptibilities are observed as the size ratio is increased and the shifts due to the geometrical shape effects are especially important for the smaller dot sizes (≤ 25 nm). The shifts are due mostly to the increasing confinement as the dot becomes more elliptical, and not due to the interaction energy between electron and hole. A splitting of the first few excited states appears in the elliptical cross section cases since the symmetry-related degeneracy of the excited states in the circular dot is broken. This gives also rise to a more monotonic decrease of the peak intensities seen as the energy of the transition increases.

ACKNOWLEDGMENTS

We would like to thank R.L. Cappelletti and D.A. Drabold for helpful discussions, and the support of the US Department of Energy through grant no. DE-FG02-91ER45334. Calculations were partially performed at the Cray Y/MP of the Ohio Supercomputer Center. S.E.U. acknowledges support of the A. v. Humboldt Foundation.

APPENDIX:

The Coulomb interaction matrix elements of the electron-hole pair can be calculated analytically using the harmonic-oscillator basis sets we use. With the basis set in Eq. (4), one can write

$$\begin{aligned} \langle n_x', n_y' | \frac{e^2}{\epsilon \sqrt{x^2 + y^2}} | n_x, n_y \rangle &= \frac{e^2}{\epsilon \pi} \sqrt{\frac{\mu \omega_x}{\hbar}} \sqrt{\frac{\mu \omega_y}{\hbar}} (2^{n_x' + n_x + n_y' + n_y} n_x'! n_x! n_y'! n_y!)^{-1/2} \\ &\times \int_{-\infty}^{\infty} \int_{-\infty}^{\infty} dx dy e^{-(\frac{\mu \omega_x}{\hbar} x^2 + \frac{\mu \omega_y}{\hbar} y^2)} \frac{1}{\sqrt{x^2 + y^2}} \\ &\times H_{n_x'}(\sqrt{\frac{\mu \omega_x}{\hbar}} x) H_{n_x}(\sqrt{\frac{\mu \omega_x}{\hbar}} x) H_{n_y'}(\sqrt{\frac{\mu \omega_y}{\hbar}} y) H_{n_y}(\sqrt{\frac{\mu \omega_y}{\hbar}} y). \end{aligned} \quad (\text{A1})$$

As the Hermit polynomials are represented by,¹⁷

$$H_{n_x}(\sqrt{\frac{\mu \omega_x}{\hbar}} x) = \sum_{\beta=0}^{n_x/2} (-1)^\beta 2^{n_x-2\beta} \left(\frac{\mu \omega_x}{\hbar}\right)^{\frac{n_x-2\beta}{2}} \frac{n_x!}{\beta! (n_x - 2\beta)!} x^{n_x-2\beta}, \quad (\text{A2})$$

one can write,

$$\begin{aligned} \langle n_x', n_y' | \frac{e^2}{\epsilon \sqrt{x^2 + y^2}} | n_x, n_y \rangle &= \frac{e^2}{\epsilon \pi} \sqrt{\frac{\mu \omega_x}{\hbar}} \sqrt{\frac{\mu \omega_y}{\hbar}} (2^{n_x' + n_x + n_y' + n_y} n_x'! n_x! n_y'! n_y!)^{-1/2} \\ &\times \sum_{\alpha=0}^{[n_x'/2]} \sum_{\beta=0}^{[n_x/2]} \sum_{\gamma=0}^{[n_y'/2]} \sum_{\delta=0}^{[n_y/2]} \frac{(-1)^{\alpha+\beta+\gamma+\delta} n_x'! n_x! n_y'! n_y!}{\alpha! (n_x' - 2\alpha)! \beta! (n_x - 2\beta)! \gamma! (n_y' - 2\gamma)! \delta! (n_y - 2\delta)!} \\ &\times \left(\frac{\mu \omega_x}{\hbar}\right)^{\frac{n_x' + n_x - 2\alpha - 2\beta}{2}} \left(\frac{\mu \omega_y}{\hbar}\right)^{\frac{n_y' + n_y - 2\gamma - 2\delta}{2}} 2^{n_x' + n_x + n_y' + n_y - 2\alpha - 2\beta - 2\gamma - 2\delta} \\ &\times \int_{-\infty}^{\infty} \int_{-\infty}^{\infty} dx dy e^{-(\frac{\mu \omega_x}{\hbar} x^2 + \frac{\mu \omega_y}{\hbar} y^2)} \frac{1}{\sqrt{x^2 + y^2}} x^{n_x' + n_x - 2\alpha - 2\beta} y^{n_y' + n_y - 2\gamma - 2\delta}. \end{aligned} \quad (\text{A3})$$

Here, the integral factor,

$$I = \int_{-\infty}^{\infty} \int_{-\infty}^{\infty} dx dy e^{-\left(\frac{\mu\omega_x}{\hbar}x^2 + \frac{\mu\omega_y}{\hbar}y^2\right)} \frac{1}{\sqrt{x^2 + y^2}} x^{n_{x'}+n_x-2\alpha-2\beta} y^{n_{y'}+n_y-2\gamma-2\delta},$$

can be transformed to polar coordinates, so that,

$$\begin{aligned} I &= \int_0^{2\pi} d\varphi \left[\int_0^{\infty} dr e^{-(ar^2 \cos^2 \varphi + br^2 \sin^2 \varphi)} r^{l+m} \right] \cos^l \varphi \sin^m \varphi \\ &= (-1)^{2l+m} \Gamma(n) \frac{1}{a^n} \frac{\Gamma(\frac{l+1}{2}) \Gamma(\frac{m+1}{2})}{\Gamma(\frac{l+m}{2} + 1)} F\left(\frac{m+1}{2}, n; \frac{l+m}{2} + 1; \frac{a-b}{a}\right), \end{aligned} \quad (\text{A4})$$

where $a = \mu\omega_x/\hbar$, $b = \mu\omega_y/\hbar$, $l = n_{x'} + n_x - 2\alpha - 2\beta$, $m = n_{y'} + n_y - 2\gamma - 2\delta$, and $n = \frac{1}{2}(l + m + 1)$.

The interaction matrix elements can be expressed in terms of hypergeometric functions as

$$\begin{aligned} \langle n_{x'}, n_{y'} | \frac{e^2}{\epsilon \sqrt{x^2 + y^2}} | n_x, n_y \rangle &= \frac{e^2}{\epsilon \pi} \sqrt{\frac{\mu\omega_y}{\hbar}} (2^{s_x+s_y} n_x'! n_x! n_y'! n_y!)^{-1/2} \\ &\times \sum_{\alpha=0}^{[n_x'/2]} \sum_{\beta=0}^{[n_x/2]} \sum_{\gamma=0}^{[n_y'/2]} \sum_{\delta=0}^{[n_y/2]} \frac{(-1)^\eta n_x'! n_x! n_y'! n_y!}{\alpha! (n_x' - 2\alpha)! \beta! (n_x - 2\beta)! \gamma! (n_y' - 2\gamma)! \delta! (n_y - 2\delta)!} \\ &\times \left(\frac{\omega_y}{\omega_x} \right)^{\frac{s_y}{2} - \gamma - \delta} (-1)^{s_y} 2^{s_x+s_y-2\eta} \\ &\times F \left[\frac{1}{2}(s_y + 1) - \gamma - \delta, \frac{1}{2}(s_x + s_y + 1) - \eta; \frac{1}{2}(s_x + s_y) - \eta + 1; 1 - \frac{\omega_y}{\omega_x} \right] \\ &\times \Gamma \left[\frac{1}{2}(s_x + s_y + 1) - \eta \right] \Gamma \left[\frac{1}{2}(s_x + 1) - \alpha - \beta \right] \Gamma \left[\frac{1}{2}(s_y + 1) - \gamma - \delta \right] / \Gamma \left[\frac{1}{2}(s_x + s_y) - \eta + 1 \right], \end{aligned} \quad (\text{A5})$$

where F is a hypergeometric function,¹⁷ $\eta = \alpha + \beta + \gamma + \delta$, and the extra constraints of $s_y = n_y + n_y' = \text{even}$, and $s_x = n_x + n_x' = \text{even}$, are required for this matrix element to be non-zero. Use of this equation in the calculation of the Coulomb matrix elements was very important in the solution of the problem, as it reduces the computation time substantially.

REFERENCES

- ¹ L. E. Brus, IEEE J. Quantum Electron. **QE-22**, 1909 (1986); J. Phys. Chem. **90**, 2555 (1986); in *Chemical Processes in Inorganic Materials: Metal and Semiconductor Clusters and Colloids*, edited by P. D. Persans, J. S. Bradley, R. R. Chianelli, and G. Schmid, MRS Symposia Proceedings No. 272 (Materials Research Society, Pittsburgh, 1992), p.215.
- ² See, e.g., C. Weisbuch and B. Vinter, *Quantum Semiconductor Structures*, Chap. V, (Academic Press, Boston, 1991).
- ³ S. Schmitt-Rink, D. S. Chemla, and D. A. B. Miller, Advances in Physics, **38**, 89 (1989).
- ⁴ G. H. Cocoletzi and S. E. Ulloa, Phys. Rev. B **49**, 7573 (1994).
- ⁵ G. W. Bryant, Phys. Rev. B **37**, 8763 (1988); Surf. Sci. **196**, 596 (1988).
- ⁶ Y. Z. Hu, M. Lindberg, and S. W. Koch, Phys. Rev. B **42**, 1713 (1990); Y. Z. Hu, S. W. Koch, M. Lindberg, N. Peyghambarian, E. L. Pollock, and F. F. Abraham, Phys. Rev. Lett. **64**, 1805 (1990).
- ⁷ W. Que, Phys. Rev. B **45**, 11036 (1992).
- ⁸ V. Halonen, T. Chakraborty, and P. Pietiläinen, Phys. Rev. B **45**, 5980 (1992).
- ⁹ K. Brunner, G. Abstreiter, G. Böhm, G. Tränkle, and G. Weimann, Phys. Rev. Lett. **73**, 1138 (1994).
- ¹⁰ K. Brunner, U. Bockelmann, G. Abstreiter, M. Walther, G. Böhm, G. Tränkle, and G. Weimann, Phys. Rev. Lett. **69**, 3216 (1992).
- ¹¹ S. Schmitt-Rink, D. A. B. Miller, and D. S. Chemla, Phys. Rev. B **35**, 8113 (1987).
- ¹² S. Fafard, D. Leonard, J. L. Merz, and P. M. Petroff, Appl. Phys. Lett. **65**, 1388 (1994).
- ¹³ J. Y. Marzin, J. M. Gérard, A. Izraël, D. Barrier, and G. Bastard, Phys. Rev. Lett. **73**, 716 (1994).

- ¹⁴ J. M. Moison, F. Houzay, F. Barthe, and L. Leprince, Appl. Phys. Lett. **64**, 196 (1994).
- ¹⁵ J. Y. Marzin and G. Bastard, Solid State Commun. **92**, 437 (1994).
- ¹⁶ We neglect the possible hole-band mixing occurring especially in the smallest of quantum dots ($\leq 3 - 5$ nm) [see, e.g., D. Broido and L.J. Sham, Phys. Rev. B **31**, 888 (1985)]. This is expected to produce only a small shift of the hole energy states, especially for the larger dots, and it greatly simplifies calculations.
- ¹⁷ *Handbook of Mathematical Functions*, M. Abramowitz and I. A. Stegun (Dover, New York, 1972).
- ¹⁸ C. Hermann and C. Weisbuch, Phys. Rev. B **15**, 823 (1977).
- ¹⁹ W. L. Mochán and R. G. Barrera, Phys. Rev. B **32**, 4984 and 4989 (1985).
- ²⁰ *Numerical Recipes in Fortran*, edited by W. H. Press, S. A. Teukolsky, W. T. Vetterling, and B. P. Flannery (Cambridge University Press, New York, 1992). Notice that QL stand for orthogonal and lower triangular transformations.

FIGURES

FIG. 1. GaAs quantum dot. (a) Exciton binding energy; (b) normalized electron-hole separation as function of the quantum dot size for elliptical quantum dots with several size ratios in the xy plane. $L_x : L_y$ shown are 1:1 to 2:1, and 3:1, with diamonds, pluses, and triangles, respectively. Insets: Solid, dot, dashed, and dashed-dot curves are the results for circular case and $M = 30$, 100, and 500 basis sets, respectively. Diamonds show results for the $M = 400$ Ω basis set with optimized frequency, while triangles are for $M = 400$ in the original ω basis. Inset in (a) also shows (scale on the right) the value of $E_\Omega = \hbar\Omega$ used in the calculation.

FIG. 2. Imaginary part of linear optical susceptibility for a GaAs elliptic quantum dot with the same area but different axis ratios, as a function of frequency. Bottom trace is for a circular dot, $L_x = L_y = 5$ nm. Upper two traces show results for elliptical dots with size ratios $L_y : L_x = 2 : 1$ ($L_y = 7.0$ nm and $L_x = 3.5$ nm), and 3:1 ($L_y = 8.7$ nm and $L_x = 2.9$ nm), respectively.

FIG. 3. Same as Fig. 2 but for a size $L = 10$ nm.

FIG. 4. Imaginary part of linear optical susceptibility for InAs elliptic quantum dots with lateral mean size 12 nm and thickness 2.8 nm (with $\Gamma = 2.0$ meV), as a function of frequency. The bottom trace is for a circular dot with $L_x = L_y = 12$ nm. The upper two traces show results for elliptical dots with a size ratio $L_y : L_x = 2 : 1$ ($L_y = 17$ nm and $L_x = 8.5$ nm), and 3:1 ($L_y = 20.7$ nm and $L_x = 6.9$ nm), respectively. Notice the similarity with Fig. 2.

Fig. 1
 Geometrical confinement effects on excitons...
 J. Song and S.E. Ulloa

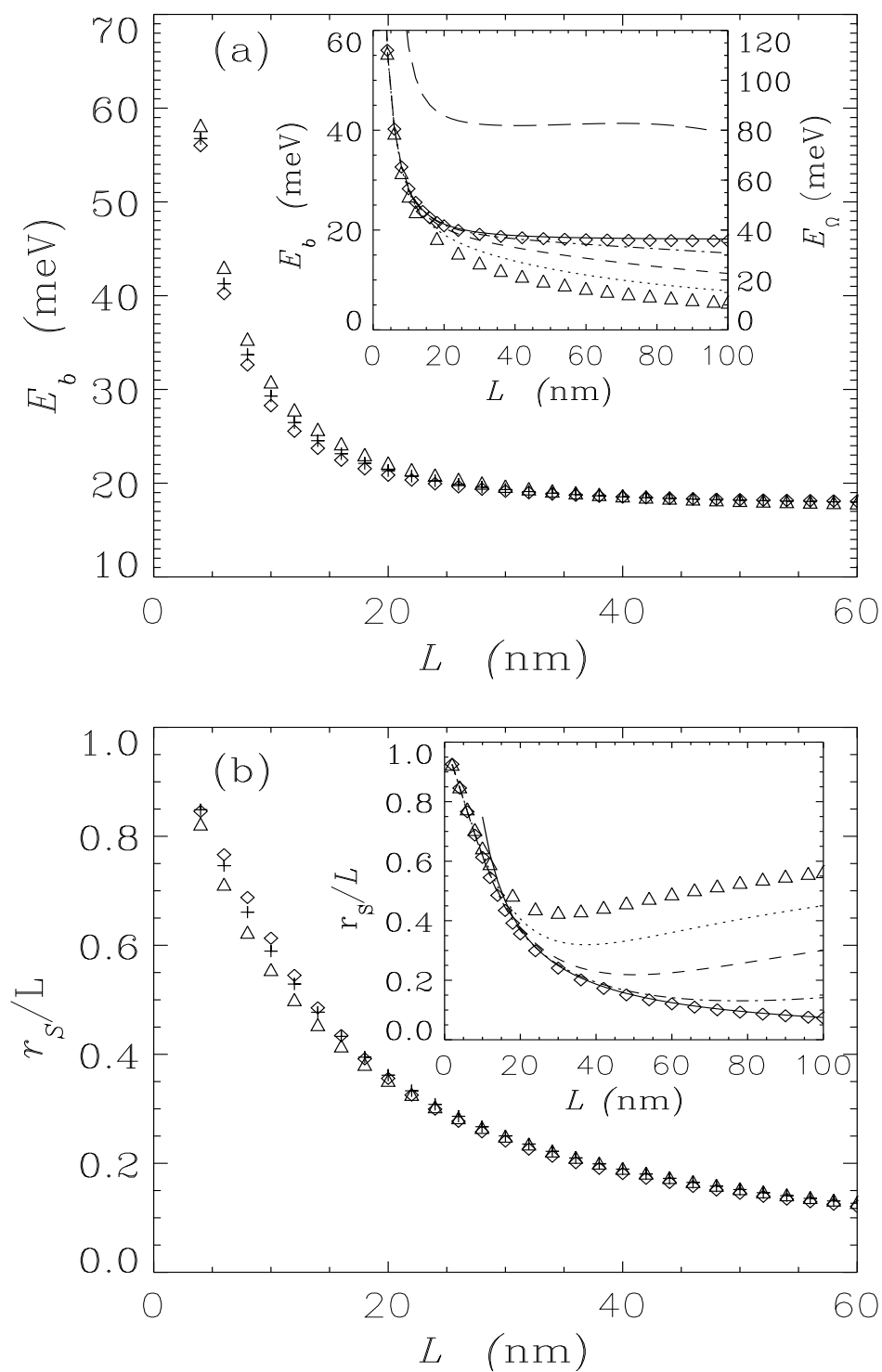


Fig. 1

Fig. 2
Geometrical confinement effects on excitons...
J. Song and S.E. Ulloa

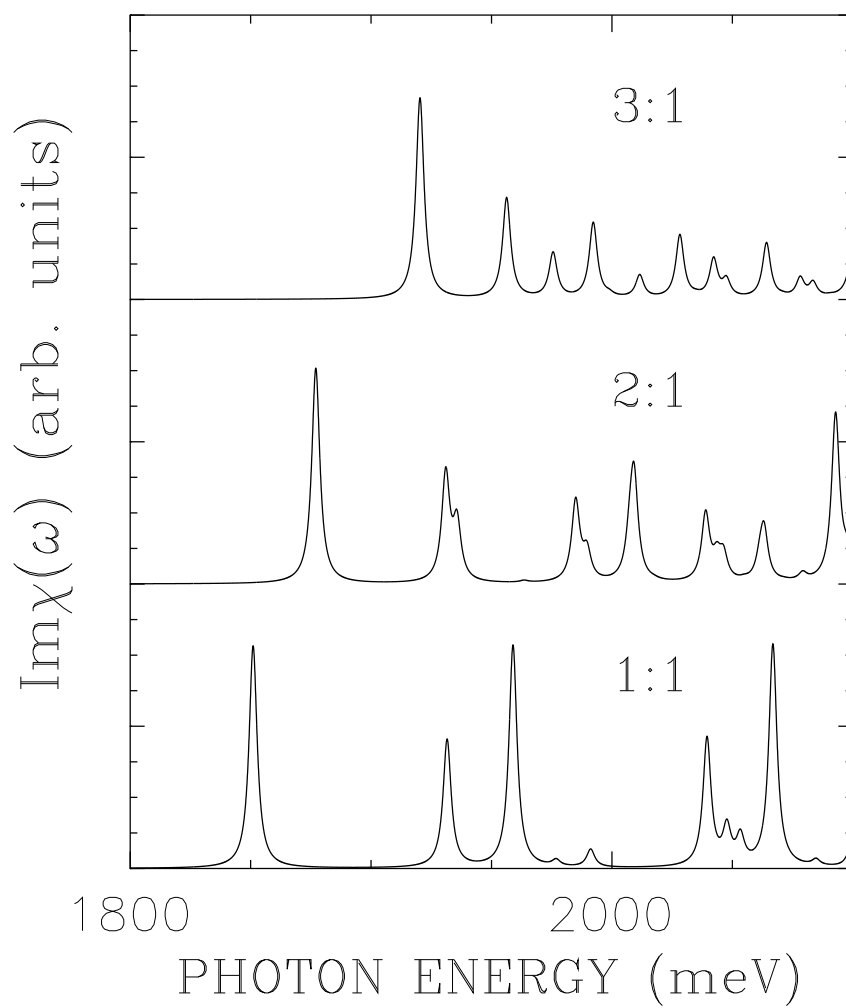


Fig. 2

Fig. 3
Geometrical confinement effects on excitons...
J. Song and S.E. Ulloa

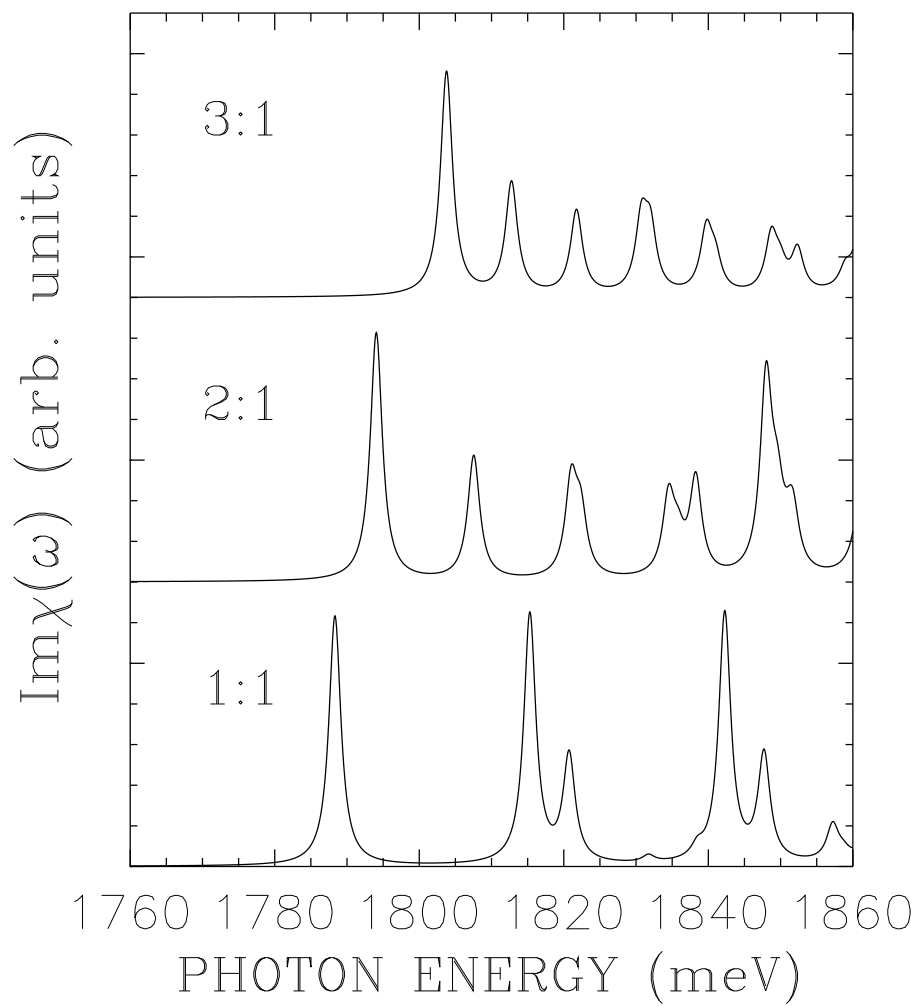


Fig. 3

Fig. 4
Geometrical confinement effects on excitons...
J. Song and S.E. Ulloa

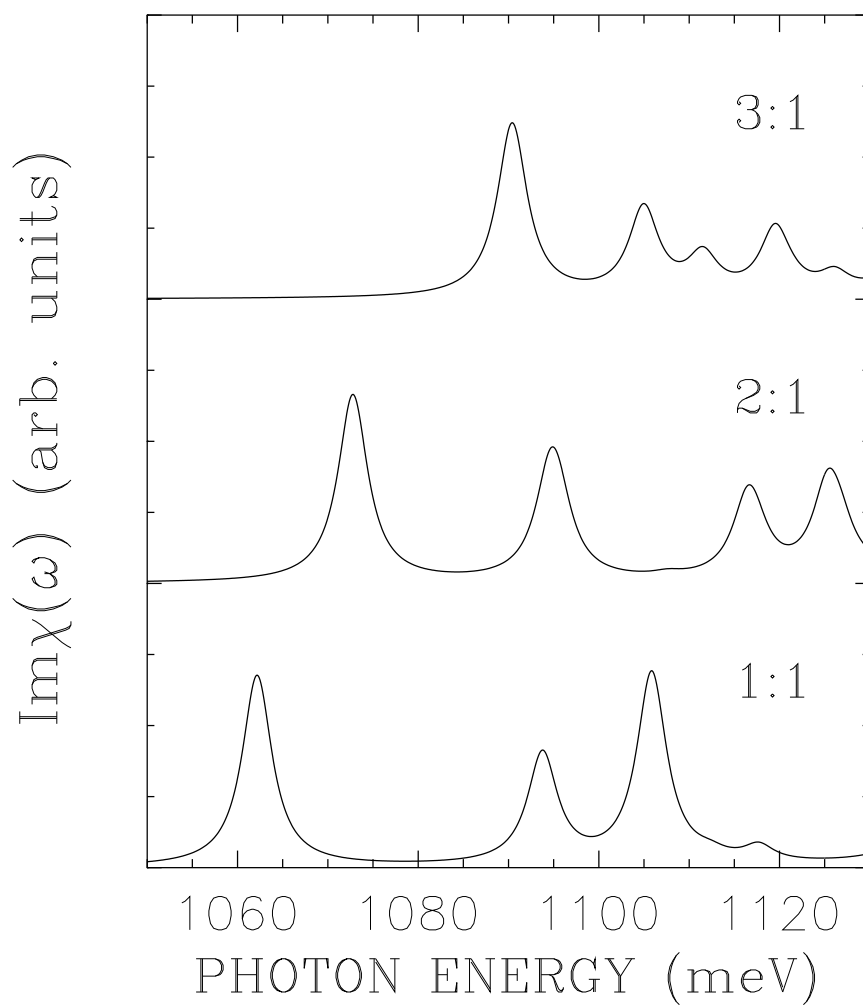


Fig. 4